Check for updates

Luminescence characteristics of rare-earth-doped barium hexafluorogermanate BaGeF$_6$ nanowires: fast subnanosecond decay time and high sensitivity in H$_2$O$_2$ detection†

Gibin George,[a] Machael D. Simpson,[a] Bhoj R. Gautam,[a] Dong Fang,[b] Jinfang Peng,‡[c] Jianguo Wen,[c] Jason E. Davis,[d] Daryush Ila[a] and Zhiping Luo [ID] *[a]

Fluorides are promising host materials for optical applications. This paper reports the photoluminescent (PL) and cathodoluminescent (CL) characteristics of barium hexafluorogermanate BaGeF$_6$ nanowires codoped with Ce^{3+}, Tb^{3+} and Sm^{3+} rare earth ions, produced by a solvothermal route. The synthesized BaGeF$_6$ nanowires exhibit uniform morphology and size distribution. X-ray diffraction divulges the one-dimensional growth of crystalline BaGeF$_6$ structure, with the absence of any impurity phases. Visible luminescence is recorded from the nanowires in green and red regions, when the nanowires are codoped with Ce^{3+}/Tb^{3+}, and Ce^{3+}/Tb^{3+}/Sm^{3+}, respectively, under a UV excitation source. The PL emission from the codoped BaGeF$_6$ nanowires, when excited by a 254 nm source, originates from the efficient energy transfer bridges between Ce^{3+}, Tb^{3+} and Sm^{3+} ions. The decay time of the visible luminescent emission from the nanowires is in the order of subnanoseconds, being one of the shortest decay time records from inorganic scintillators. The CL emission from the BaGeF$_6$ nanowires in the tunable visible range reveals their potential use for the detection of high-energy radiation. The PL emissions are sensitive to H$_2$O$_2$ at low concentrations, enabling their high-sensitivity detection of H$_2$O$_2$ using BaGeF$_6$ nanowires. A comparison with BaSiF$_6$ nanowires is made in terms of decay time and its sensitivity towards H$_2$O$_2$.

Introduction

The luminescent property of a material may be significantly altered when it is prepared within a nanoscale domain, and further changes may be made by tailoring its morphology and doping. High luminescence has been reported for nanosized architectures with high aspect ratios, e.g., nanowires, nanofibers, nanorods, and nanowhiskers, etc., as they can guide the emission to the detector more efficaciously than bulk or other forms of architecture, when they are preferentially oriented.[1–4] Fluorides are iconic materials for optical related applications

[a]Department of Chemistry and Physics, Fayetteville State University, Fayetteville, NC 28301, USA. E-mail: zluo@uncfsu.edu

[b]College of Materials Science and Engineering, Kunming University of Science and Technology, Kunming 650093, P. R. China

[c]Centre for Nanoscale Materials, Argonne National Laboratory, Argonne, Illinois 60439, USA

[d]Oak Ridge Institute for Science and Education, Oak Ridge Associated Universities, Oak Ridge, TN 37830, USA

† Electronic supplementary information (ESI) available: Low-magnification image of BaGeF$_6$ nanowires, EDS results of BaGeF$_6$ nanowires, mechanism of energy transfer, PL spectra of binary doped BaGeF$_6$ nanowires and photographs of PL emission at different doping. See DOI: 10.1039/c8ra07806h

‡ Present address: Southwest Jiaotong University, Chengdu 610031, P. R. China.

due to their high quantum efficiency, high resistivity,[5] a large optical-transmission domain and lower phonon energies, which in turn reduce the probability of non-radiative quenching from the excited states as compared to other halides or oxides.[6] Although the photoluminescent (PL) emission from the pure fluoride matrices are in the near UV band, these materials are widely explored as fluorescent host matrices for rare-earth (RE) ions. RE^{3+} doping improves/tailors the luminescence of the host; however, the host also plays vital roles in tuning the luminescence emission bands of several RE^{3+} ions, since the crystal field of the host lattice and the local symmetry of the dopant in the crystal lattice determine the energy level splitting of the emissive ions.[7] Besides the low power excitation, RE-doped materials exhibit sharp emissions, long lifetime, excellent photo-stability and large Stokes shift.[8] These unique properties of RE^{3+} ions are connected to the electronic configuration in f-block elements, wherein, the 4f electrons in inner shells are shielded by the 5s and 5p subshells.[9]

PL properties of the fluorides have gained intense research recently. RE^{3+}-doped luminescent fluorides are envisaged for optical storage, biological labelling, non-invasive imaging, solid-state lasers, light-emitting diodes, theranostics/theragnostics, up-conversion lasers, solar cells, spectrum

modifiers, photodynamic therapy remote controllers, optical waveguide amplifiers and temperature sensors.[10] Moreover, fluorides have been widely used as wide-band gap insulating overlayers, gate dielectrics, insulators, and buffer layers in semiconductor-on-insulator structures in microelectronics and optoelectronic devices.[11] Mn^{4+}-activated complex fluorides, ABF_6 phosphors (A = divalent element, B = tetravalent element), e.g., $BaSiF_6$,[12] $BaGeF_6$,[13] $BaTiF_6$,[14] $BaSnF_6$,[15] etc. and A_2BF_6 (A = monovalent element, B = tetravalent element) phosphors, e.g., K_2TiF_6,[16] K_2SiF_6,[17] K_2GeF_6,[18] Na_2SiF_6,[19] Na_2GeF_6,[20] Na_2TiF_6,[21] etc., are introduced as red emitting phosphors when excited by a blue light with better color rendering properties suitable for warm-white LED devices in the recent years, as replacements of conventional Ce^{3+}:YAG phosphors.

Though Mn^{4+}-doped complex hexafluorides are extensively studied as red phosphors, very little is known about the potentiality of these materials as the host matrices for RE ions and their structural and optical properties, although, Eu^{3+}- and Sm^{3+}-doped fluorides are also potential red emitting phosphors with a high color rendering index. But, the absorption bands of Eu^{3+} and Sm^{3+} ions are very narrow in blue or near-UV region, which is attributed to the parity-forbidden 4f–4f transitions. The absorptions bands of these red emitting RE^{3+} ions can be broadened by codoping with other RE^{3+} ions with broad absorption bands as sensitizers, for instance Ce^{3+}, Tb^{3+}, Dy^{3+}, etc. Recently, we synthesized $BaSiF_6$ nanowires codoped with RE^{3+} ions for the gamut emission and these nanowires exhibit efficient PL emission under UV excitation and the decay time was in the order of hundreds of picoseconds (subnano-seconds).[22] Codoping of other complex fluorides with different luminescent RE^{3+} ions for the controlled emission has not been well addressed in literature so far. $BaGeF_6$ is one such complex fluoride, whose PL characteristics are exclusively reported as a red-light emitting phosphor for warm white LED devices when doped with Mn^{4+} ions in the recent years.[13,23,24] The PL emission properties of Mn^{4+} doped $BaGeF_6$ red phosphors are analogous to the complex fluorides with the formula $BaXF_6$ (X = Si, Ti, Sn, etc.).[12–15] A warm white LED with a lower corrected color temperature (CCT = 4766 K) and higher color rendering index (R_a = 86.3) can be obtained by combining blue GaN chip with a mixture of $BaGeF_6$:Mn^{4+} red phosphor and commercial YAG:Ce^{3+} yellow phosphor.[24] Also, $BaGeF_6$:Mn^{4+} red phosphor exhibit good thermal stability as the phosphor can retain 42.5% of the luminescence intensity at 448 K with respect to room temperature.[24] PL and cathodoluminescent (CL) characteristics of nanosized RE^{3+}-doped $BaGeF_6$ have not been reported in the literature.

In this paper, we report the synthesis of RE-doped barium hexafluorogermanate $BaGeF_6$ (BGF) nanowires through a solvothermal method. The PL emission bands of the nanowires are tailored by Ce^{3+}, Tb^{3+} and Sm^{3+} doping and the RE^{3+} loading is optimized for efficient energy transfer between the ions, and the recorded lifetime of PL emissions are found in the order of subnanoseconds. The CL emission of these nanowires under high-energy irradiation is also studied for the potential application in high-energy radiation detection. In addition, the influences of several surrounding media on the PL characteristics of these nanowires have been studied and it is observed that the red PL emission is sensitive to H_2O_2, a reactive oxygen species, at low concentrations. H_2O_2 is used in a wide range of applications, such as disinfectant, antiseptic and oxidizer in food,[25] pharmaceutical,[26] biomedical,[27] cosmetic,[28] and chemical industries, involving biological and environmental implications.[29,30] Besides, it is a propellant in rockets,[31] and a precursor and a decomposition product of triacetone triperoxide, a progressively used explosive by terrorists.[32] Therefore, application of these inorganic luminescent nanowires as an alternative to conventional analytical probes and organic luminescent materials for the detection of H_2O_2 is promising due to their simplicity and stability.

Experimental

Preparation of pure and doped BGF nanowires

The doped and undoped nanowires are prepared using a microemulsion containing cetyltrimethylammonium bromide (CTAB) as a surfactant and 1-pentanol as co-surfactant. Cyclohexane was used as the oil phase and all the precursors were dissolved/diluted in deionized water. The chemicals used were analytical grade as received without any purification. In the synthesis process, the first step was the preparation two identical solutions of 25 mL cyclohexane containing 1 mL of 1-pentanol (Sigma Aldrich) and 2 g of CTAB (VWR International, LLC.). The pure BGF nanowires were prepared by adding 1 mL of 1 M $BaCl_2 \cdot 2H_2O$ (VWR International, LLC.) dissolved in deionized water to one of the above solutions, and 1 mL of 1 M GeO_2 (Sigma Aldrich) dissolved in 10% hydrofluoric acid (HF with concentration >40%, Sigma Aldrich) to the other solution. Both the precursor solutions were added drop wise at a rate of 2 mL h^{-1} under a vigorous stirring of 700 rpm, and the solutions became transparent after the addition. After 30 min of vigorous stirring, both the solutions were mixed together for another 10 min. The mixed solution was then transferred to 100 mL Teflon-lined autoclaves and heated at 120 °C for 12 h. After 12 h the solution was set to cool naturally to room temperature, washed with a mixture of 50% ethanol and 50% water for several times and dried at 80 °C for overnight. The doped nanowires were made using similar method, in which respective mol% of the metal chlorides $RECl_3$ were added to $BaCl_2$ solution with the subsequent replacement of $BaCl_2$ and the aforesaid procedure was followed. The samples are notated by BGF:xCe–yTb–zSm, where x, y and z are the mol% of Ce^{3+}, Tb^{3+} and Sm^{3+}, respectively.

Material characterization

The morphology of the BGF nanowires was identified using JEOL field-emission JXA-8530F Electron Probe Microanalyzer (EPMA), after coating the samples with ~5 nm carbon film (Denton carbon coater). EPMA was equipped with an X-ray Energy-Dispersive Spectrometer (EDS) for chemical compositional analysis, and an xCLent IV Advanced B Hyperspectral CL
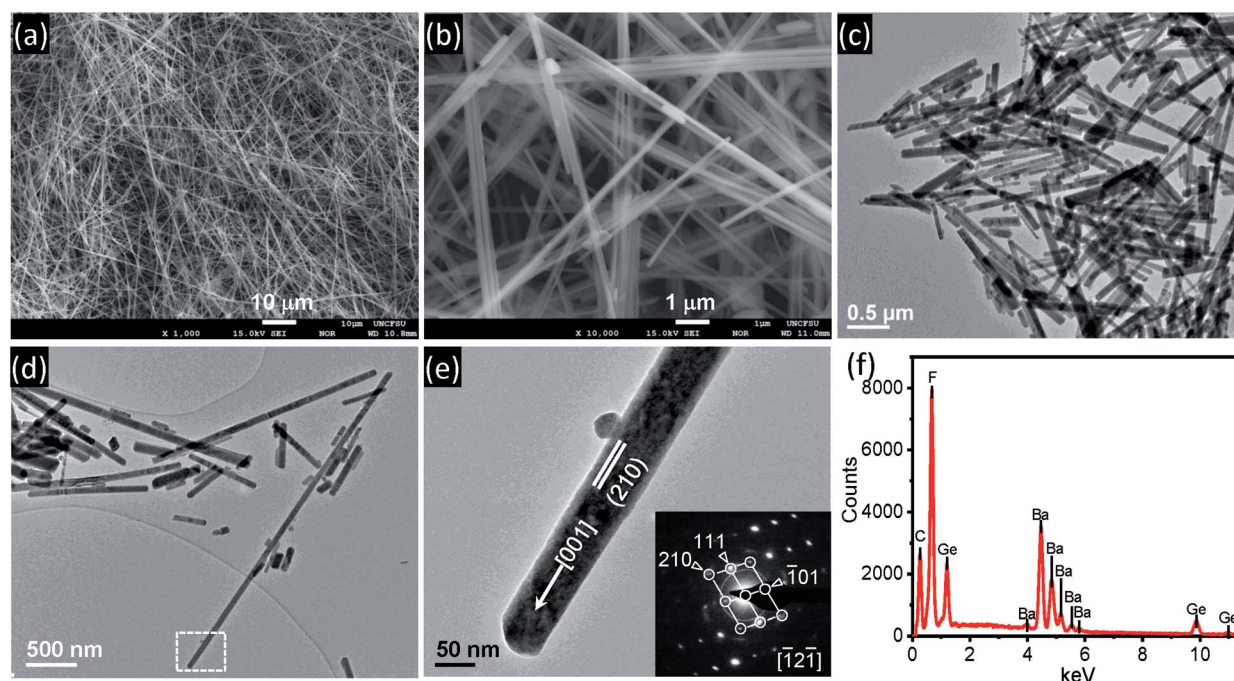
Fig. 1 Pure BGF nanowires. (a and b) SEM images in low and high magnification; (c and d) TEM images; (e) enlarged image from (d) and SAD pattern showing crystallographic direction; and (f) EDS spectrum.

Detector for the CL analysis. Samples for Transmission Electron Microscopy (TEM) were prepared in pure ethanol solutions, sonicated for 30 min to break the long nanowires and then dispersed on carbon-film supported grids. The grids were observed by using a FEI field-emission Tecnai F20ST instrument at 200 kV. The X-ray diffraction (XRD) patterns of the samples were obtained using Rigaku MiniFlex 600 X-ray diffractometer at a scanning rate of $0.075°$ min^{-1} in the range of 10–90°. The Fourier-Transform Infrared (FTIR) spectra of the samples were recorded by Shimadzu IRPrestige-21 in transmission mode by KBr pellet method in a wave number range of 4000–400 cm^{-1} for an average of 32 scans.

The PL spectra of the samples were obtained in powder form, recorded using Shimadzu RF-5301PC spectrofluorophotometer at room temperature. A time-correlated single photon counting (TCSPC) experiments were performed to measure the PL decay dynamics (Edinburgh instrument minitau). The samples were excited with 56 ps laser pulses at a wavelength of 405 nm and the emission was monitored at 594 nm. PL decay was detected using a single photon counting photomultiplier tube (PMT). The time resolution of the configuration was ~100 ps. To test the H_2O_2 sensing characteristics, 5 mg of the nanowire phosphor was dispersed in 10 mL of deionized water and the concentration of H_2O_2 was subsequently adjusted in the solution and the PL emission spectra were recorded for different concentration of H_2O_2. To test the selectivity, the PL emissions from the nanowires in the presence of 100 μM $CuSO_4(Cu^{2+})$, 100 μM $FeCl_3(Fe^{3+})$, 100 μM glucose, HCl (2 pH) and NaOH (14 pH) were recorded.

Results and discussion

Morphology and structure

The SEM images of as synthesized pure BGF nanowires are shown in Fig. 1a and b. It is observed that the size and shape of the nanowires are consistently uniform. Similar to the $BaSiF_6$ nanowires reported very recently,[22] the synthesized $BaGeF_6$ nanowires are long, typically in the range of 50–100 μm from low-magnification SEM images (Fig. 1a and S1†). The TEM images are shown in Fig. 1c and d. Without a surface coating in the TEM images, the average diameter is measured as 58 nm with a standard deviation of 12.3 nm, based on 30 measurements, giving the aspect ratio of several hundreds (Fig. S2†). A single nanowire, as marked in Fig. 1d, is magnified in Fig. 1e. A selected-area diffraction (SAD) pattern from the nanowire is inserted in Fig. 1e. At this orientation, the edge-on surface is (210), as the nanowire surface (110) is not at the edge-on orientation. However, the nanowire axis is identified as [001] direction. The EDS spectrum of pure BGF is shown in Fig. 1f that confirms the high purity of the nanowires (Table S1;† the element C is from the surface coating). A representative EDS spectrum of ternary doped nanowires is shown in Fig. S3.† TG analysis results of pure BGF nanowires is shown in Fig. S4.† The nanowires are stable up to 400 °C. However, the evaporation of adsorbed water and the crystallized water is observed until 300 °C, and then the weight is lost gradually until 600 °C by releasing a GeF_4 gas to form BaF_2 structure.[33] It is observed that the phase transformation from rhombohedral BGF to cubic BaF_2 is exothermic from the DTA curve.
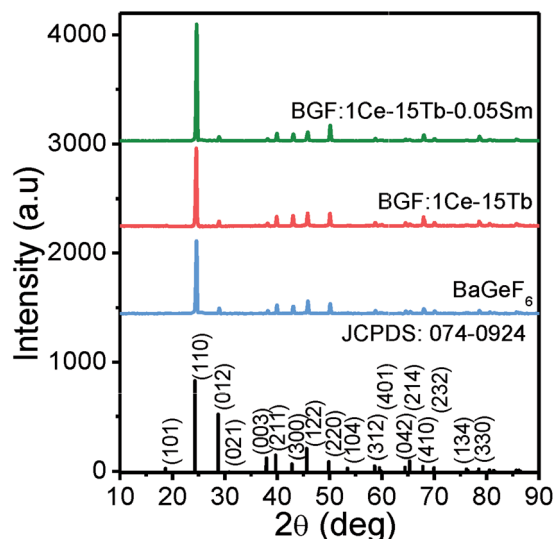
Fig. 2 The XRD patterns of the pure and doped BGF nanowires.

Fig. 3 FTIR spectra of pure and doped BGF nanowires.

Fig. 2 shows the XRD patterns of the as BGF nanowires and its RE-doped counterparts. The peaks in the XRD pattern of the nanowires is indexed to that of BGF (JCPDS data file no. 074-0924), which has a rhombohedral structure with a lattice parameter 4.948 Å. From the XRD data, pure crystalline nature of BGF nanowires can be observed, with well-defined sharp peaks with the highest intensity at (110) plane, implying the nanowires are grown along [001] direction with {110} surfaces exposed on the nanowires. The structure of BGF has a cesium chloride-like arrangement with Ba^{2+} cations and octahedrally arranged anions, GeF_6^{2-}, having a rhombohedral angle of about 98.245°. Ba^{2+} ion is nearly equidistant from twelve fluorine ions making the coordination number as 12 and the Ge^{4+} ions are coordinated with six fluoride ions octahedrally.[34] The crystal structure of BGF is described with the space group $R\bar{3}m$. All the diffraction peaks of the RE^{3+}-doped samples match with those of the pure BGF, which can be indexed to JCPDS 074-0924. Therefore, one can deduce that the crystalline structure of the doped BGF nanowires are pure, and the dopant ions occupied at the lattice sites of Ba^{2+} ions with octahedral symmetry.

The nanowires are grown in one [001] direction and the overall growth process comprises of two subsequent processes, they are nucleation and growth. The CTAB/1-pentanol in oil phase forms microemulsions around the water droplets containing the precursors. When the two transparent precursor solutions are mixed together, long slender wormlike reverse micelle are formed by joining the water droplets. On heating, the water droplets collapse and adjacent drops containing the precursor solution join and thus nucleates are formed. By maintaining at a temperature above the ambient temperature, nucleates are grown as wires and the wire like morphology is retained under the restrain of CTAB/1-pentanol microemulsion. The overall chemical reactions involved in the formation of nanowires are:
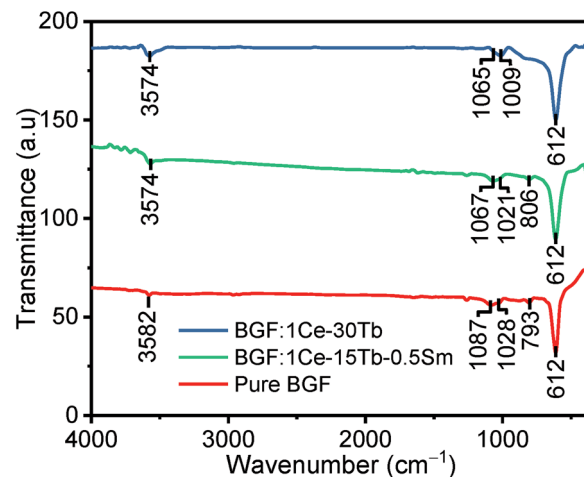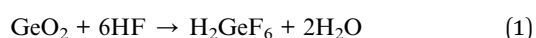
$$GeO_2 + 6HF \rightarrow H_2GeF_6 + 2H_2O \quad (1)$$

$$H_2GeF_6 + BaCl_2 \cdot 2H_2O \rightarrow BaGeF_6 + 2HCl + 2H_2O \quad (2)$$

The FTIR spectra of the as obtained samples are shown in Fig. 3. The FTIR spectra of all doped samples are analogous to pure BGF. There is no evidence of the peaks arising from the precursors used during the synthesis of the sample. The high intensity peak at 612 cm^{-1} is arising from the stretching of octahedral GeF_6^{2-} ions.[35] The peak at 3574 and 3582 cm^{-1} is attributed of –OH stretching from the adsorbed water and at 1,087, 1028 and 793 cm^{-1} can be attributed to several modes of vibrations in GeF_6^{2-} ions.[36] The significant shift of the peaks at 1087 and 1028 cm^{-1} of pure BGF samples to lower wavenumbers in doped BGF nanowires reveal the change in bond length in them, due to the difference in the electronegativity of the dopants and the Ba^{2+} ions. Moreover, the charge compensation between the trivalent RE^{3+} ions and the divalent Ba^{2+} ions is through defects such as interstitial fluoride ions and/or defect aggregations.[37]

Photoluminescence characteristics

The photoluminescence excitation (PLE) and PL spectra of unary, binary and ternary doped BGF nanowires are shown in Fig. 4. On comparing the PLE spectra of these RE^{3+}-doped nanowires, one can observe that the excitation bands of ternary doped nanowires contain all excitation bands of individual RE^{3+} ions. The PLE spectrum of BGF:2Ce nanowires exhibits an absorption peak at 231 nm for the emission monitored at 336 nm, which is characteristic to the host absorption and the peaks at 254 and 280 nm are arising from 4f → 5d ^{2}D multiplets transition of Ce^{3+} ions. The PL spectrum of BGF:2Ce nanowires displays a broad asymmetric emission band which constitutes two peaks in the UV region, when excited by a 254 nm source. In the BGF host matrix, Ce^{3+} ions replace Ba^{2+} ions with octahedral symmetry (D_{3d} point symmetry[38]) and the crystal field splitting of 4f ground state in Ce^{3+} ion in the octahedral field is $^2F_{5/2}$ and $^2F_{7/2}$, respectively.[39] One can expect two distinct emitting centers, as there are two ground state crystal field splitting and if the Ce^{3+} ions are close enough to form aggregates and the
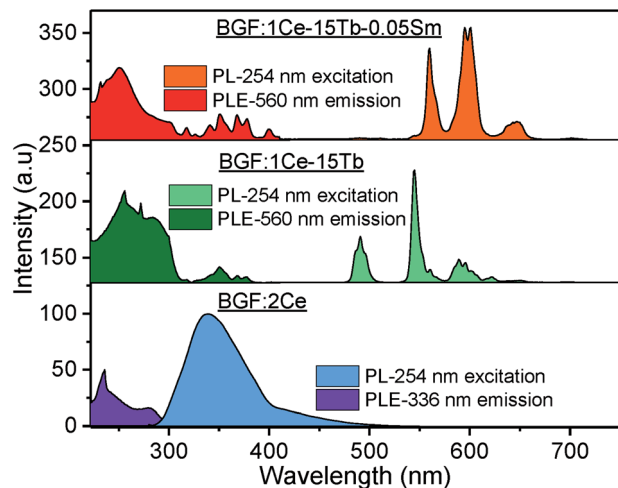
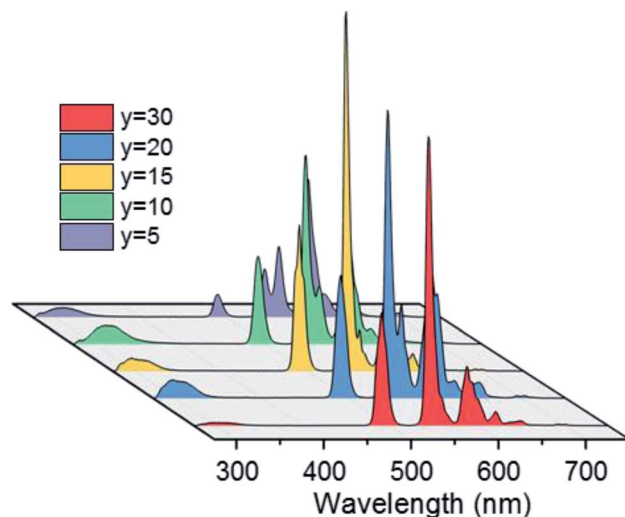**Fig. 4** PLE (left) and PL (right) spectra of representative unary, binary and ternary doped BGF nanowires.

Fig. 5 PL spectra of BGF:1Ce–yTb nanowires under 254 nm excitation.

emission arises from different local structures and the respective emissions can be intense and broad.

On Ce^{3+} and Tb^{3+} codoping, PLE spectrum monitored at 544 nm emissions, exhibit several bands between 225–400 nm originated by $4f^8 \rightarrow 4f^7 5d^1$ transition of Tb^{3+} ions.[40] The broad excitation bands between 220–300 nm are due to 4f–5d transitions and the small peaks between 300–400 nm are due to 4f–4f transitions of Tb^{3+} ions. In the corresponding PL spectrum, the sharp peaks observed at 488, 544, 590 and 620 nm are originated from $^5D_4 \rightarrow {}^7F_6$, $^5D_4 \rightarrow {}^7F_5$, $^5D_4 \rightarrow {}^7F_4$, and $^5D_4 \rightarrow {}^7F_3$ 4f–4f transitions of Tb^{3+} ions, respectively.[41] On comparing the PLE spectrum of BGF:1Ce–15Tb with that of BGF:1Ce–15Tb–0.05Sm nanowires, several additional peaks appeared in the latter, due to $^6H_{5/2} \rightarrow {}^4D_{3/2}$ (364 nm), $^6H_{5/2} \rightarrow {}^6P_{7/2}$ (378 nm), $^6H_{5/2} \rightarrow {}^4F_{7/2}$ (403 nm) and $^6H_{5/2} \rightarrow (^6P, {}^4P)_{5/2}$ transitions of Sm^{3+} ions.[42] As the excitation peaks are spanning in the UV region in the PLE spectrum, it can be concluded that both high and low energy UV light can be used as the excitation source of theses nanowires. Additionally, one can observe the overlapping of emission bands of Ce^{3+} with the excitation bands of Tb^{3+} and the emission bands of Tb^{3+} with the excitation bands of Sm^{3+}, disclosing the apparent resonance type energy transfer between these ions.[43] A detailed schematic of energy transfer bridge between Ce^{3+}–Tb^{3+}–Sm^{3+} ions is shown in Fig. S5.†

PL spectra of BGF:1Ce–yTb nanowires are shown in Fig. 5. The PL spectra consist of the weak emission peaks of Ce^{3+} ions in the UV region and the strong characteristic peaks of Tb^{3+} ions originated from 4f–4f transitions, when excited by 254 nm wavelength source. Even though, the weak 5d–4f UV emissions of Ce^{3+} ions are slightly changed with a subsequent change in the Tb^{3+} ion concentration, the significant sharp 4f–4f green emissions of Tb^{3+} ions are evident at every concentration of Tb^{3+} ions while the doping level of Ce^{3+} ions are kept constant as 1 mol%. Therefore, the corresponding spectra shown in Fig. 5 indicate the nonradiative energy transfer from Ce^{3+} to Tb^{3+} ions when doped in BGF matrix. The intensity of emission from Tb^{3+} ions are gradually increased with Tb^{3+} concentration and the

most intense emission is observed from the nanowires doped with 15 mol% of Tb^{3+} ions, and thereafter the intensity is dropped. The emission lines from Ce^{3+} ions are completely vanished when Tb^{3+} doping level is increased to 30 mol%. The reduction in Tb^{3+} emission intensity at higher concentration above 15 mol% could be attributed to Tb^{3+}–Tb^{3+} internal concentration quenching, during which the excitation energy is lost by the energy migration among the activator ions. The calculated energy transfer efficiency[44] is more than ~80% in all the Ce^{3+} and Tb^{3+} codoped nanowires, which could be accompanied to the low lattice phonon energy of the fluoride matrices. In addition, the emission from these binary doped nanowires does not alter significantly by changing the Ce^{3+} content (Fig. S6†).

In the PL spectra of BGF:1Ce–15Tb–zSm nanowires as shown in Fig. 6, strong emissions in the orange-red band are observed. These emission bands are corresponding to $^4G_{5/2} \rightarrow {}^6H_J$ transitions of Sm^{3+} ions, under an excitation of 254 nm source. More
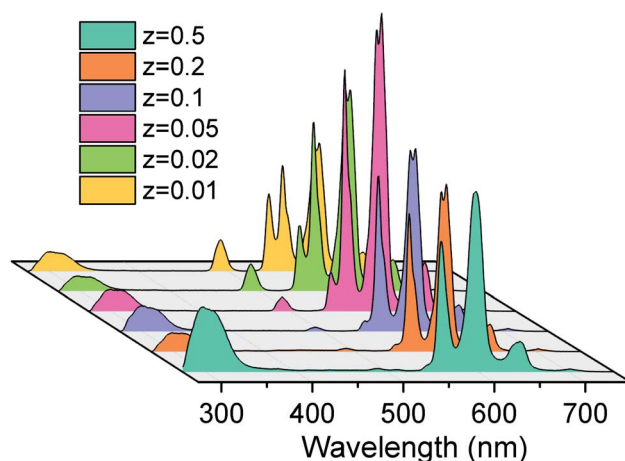

Fig. 6 PL spectra of BGF:1Ce–15Tb–zSm nanowires under 254 nm excitation.

precisely, the major emission bands peaking at 565, 604, and 653 nm are assigned to the $^4G_{5/2} \rightarrow {}^6H_{5/2}$, $^4G_{5/2} \rightarrow {}^6H_{7/2}$, and $^4G_{5/2} \rightarrow {}^6H_{9/2}$ electronic transitions of Sm^{3+} ions, respectively.[45] The intensities of the emission from the Tb^{3+} ions are completely disappeared (when z = 0.5, 0.25, and 0.1) or insignificant (when z = 0.05, 0.02 and 0.01) in the presence of Sm^{3+} ions. The intensity of the orange-red emission is increased when the Sm^{3+} content is increased from 0.01 to 0.05 mol% and then decreased above 0.05 mol%, while the concentrations of Ce^{3+} and Tb^{3+} are kept constant. The weak emission line from Ce^{3+} ions at 335 nm is appeared in the spectra at all the concentrations. The characteristic emission lines of Sm^{3+} ions are very sensitive to its concentration. Increasing the concentration of Sm^{3+} ions above 0.5 mol% reduces the intensity of characteristic emission lines from Sm^{3+} ions to a large extend, as in Fig. S7,† due to the concentration quenching. Interestingly, a well-defined characteristic emission of Sm^{3+} ions did not appear, when the BGF nanowires are binary doped with Ce^{3+}/Sm^{3+} or Tb^{3+}/Sm^{3+}, as in Fig. S8,† indicating the absence of a charge transfer bridge in those phosphors. The green emissions from Ce^{3+}/Tb^{3+} and orange-red emissions from $Ce^{3+}/Tb^{3+}/Sm^{3+}$ doped BGF nanowires can be clearly distinguished from the photographs of the nanowire phosphor dispersions in water under 254 nm UV excitation, as shown in Fig. S9.†

The binary and ternary codoped BGF nanowires exhibit emission under 350 nm source, as shown in Fig. 7a and b, respectively. One can manifest the several excitation bands from the PLE spectra as shown in Fig. 4. The broad blue emission is accustomed to the $^5D_3 \rightarrow {}^7F_j$ (j = 2, 3, 4) transitions of Tb^{3+} ions due to the relaxation of the ions excited by the direct source band and the orange-red emission bands can be ascribed to the $^4G_{5/2} \rightarrow {}^6H_J$ transition of Sm^{3+} ions. The $^5D_3$ blue emission of Tb^{3+} is the highest when the concentration of Tb^{3+} is 5 mol% and it is decreased with the increase of Tb^{3+} content. In the case of ternary doped nanowires, as the Sm^{3+} content is 0.05 mol% or higher, the blue emission is the highest for a constant 1 mol% Ce^{3+} and 15 mol% Tb^{3+} doping, but it is reduced by increasing the Tb^{3+} content to 20 or 30 mol% as shown in Fig. 7b. This blue emission is not observed when excited by 254 nm source

Table 1 CIE Coordinates calculated from the PL spectra of codoped BGF nanowire phosphors

Sl no.	Sample composition	CIE (x)	CIE (y)
1	BGF:1Ce–5Tb	0.321	0.309
2	BGF:1Ce–10Tb	0.313	0.382
3	BGF:1Ce–15Tb	0.303	0.478
4	BGF:1Ce–20Tb	0.343	0.413
5	BGF:1Ce–30Tb	0.318	0.538
6	BGF:3Ce–10Tb	0.309	0.378
7	BGF:1Ce–15Tb–0.01Sm	0.368	0.356
8	BGF:1Ce–15Tb–0.02Sm	0.377	0.354
9	BGF:1Ce–15Tb–0.05Sm	0.254	0.173
10	BGF:1Ce–20Tb–0.05Sm	0.405	0.345
11	BGF:1Ce–30Tb–0.05Sm	0.415	0.366
12	BGF:1Ce–15Tb–0.1Sm	0.353	0.304
13	BGF:1Ce–15Tb–0.25Sm	0.256	0.195
14	BGF:1Ce–20Tb–0.05 Sm	0.282	0.244

because the emission originate by the relaxation from $^5D_3$ level is quenched by the cross-relaxation process, *i.e.*, $Tb^{3+}(^5D_3) + Tb^{3+}(^7F_6) \rightarrow Tb^{3+}(^5D_4) + Tb^{3+}(^7F_0)$ accompanied by the subsequent enhancement of the emissions from the $^5D_4$ level.[46]

The CIE diagrams and the corresponding coordinates of the nanowires when excited by 350 nm source are presented in Fig. S10† and Table 1, respectively. The emission from the nanowires can be tailored from blue, green and red region through white light by varying the level of doping. A slight change in the Sm^{3+} doping causes a significant change in the overall emission from red to blue. Therefore, a meticulous control on the dopant composition is required to produce blue, red, and white light emission from the nanowires.

Photoluminescence decay dynamics

The time-resolved luminescent decay analysis of binary and ternary doped BGF nanowires are shown in Fig. 8. The lifetime for the intense emission at 544 nm from BGF:1Ce–yTb nanowires and 602 nm from BGF:1Ce–yTb–zSm is analyzed and presented in Table 2. The decay curves are fitted to three
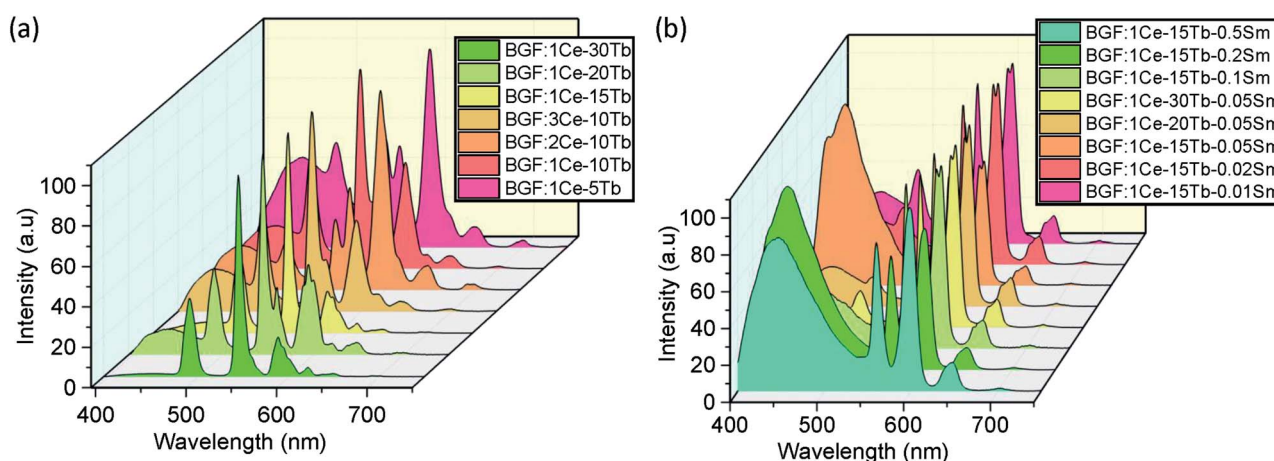

Fig. 7 PL spectra of codoped BGF nanowires excited by 350 nm wavelength.
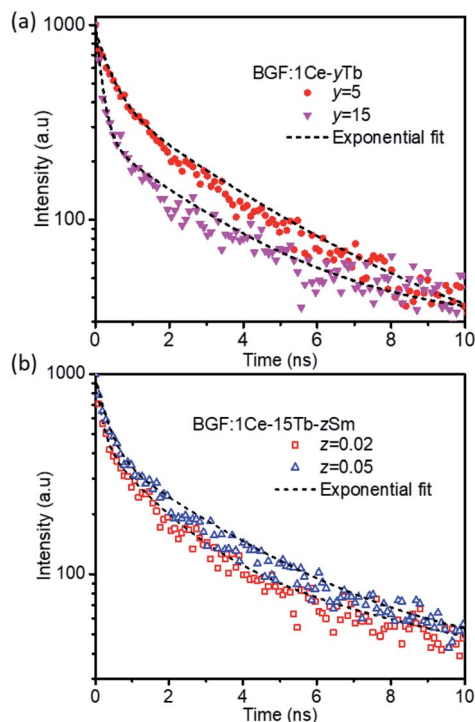
Fig. 8 Lifetime curves of representative (a) BGF:1Ce−yTb and (b) BGF:1Ce−15Tb−zSm nanowires.

component exponential function as in eqn (3), as the adjusted R^2 values are remarkably higher than the two-component fit.

$$I(t) = \alpha_1 e^{(-t/\tau_1)} + \alpha_2 e^{(-t/\tau_2)} + \alpha_3 e^{(-t/\tau_3)} \qquad (3)$$

where $I(t)$ is the light intensity at any time, t, after switching off the excitation illumination, α_i is a time-invariant constant and τ_i is a decay constant (or lifetime) for the exponential components. The estimated parameters for the respective nanowires are listed in Table 2.

Among the three components observed in the exponential fit, the first two components (τ_1 and τ_2) are remarkably faster than the third component. The fast decay time components τ_1 and τ_2 of the samples indicate two different recombination

centers one on the distorted lattice sites close to the surface and the other from the shallow surface traps of the nanowires. While comparing the life time of BGF:xCe–yTb nanowires, as the Tb^{3+} content increases the decay lifetime is decreased monotonically, which strongly supports the energy transfer from the Ce^{3+} to Tb^{3+} ions. The non-radiative energy relaxation is significantly faster over cross-relaxation upon increasing the concentration of Tb^{3+} ions, as observed at several instances of sensitizer-activator involved luminescence.[47,48] The decay time measured for the emissions from Sm^{3+} ions in BGF:xCe–yTb–zSm nanowires are longer than those measured from Tb^{3+} ions in BGF:xCe–yTb nanowires because of the longer travel of photons through several energy exchanges. The lifetime of Sm^{3+} emission is significantly affected on increasing the Tb^{3+} content, and it is increased from 0.58 ns to 2.67 ns while increasing the Tb^{3+} content from 15 mol% to 30 mol% for a constant Ce^{3+} and Sm^{3+} doping. Moreover, a subsequent increase in decay time is observed with increasing the Sm^{3+} content while Ce^{3+} and Tb^{3+} dopants kept constant.

The decay time observed in RE^{3+}-doped BGF nanowires is several orders shorter than the decay time of Mn^{4+} doped BGF microrods, which was reported as ∼8.76 ms.[13] The decay time in inorganic materials is dependent on the dopant occupancy in the lattice sites and crystal size effect.[49] Mn^{4+} occupy a parity forbidden transition site of Ge^{4+} ions with inversion symmetry in BGF, whereas, the RE^{3+} dopants occupy Ba^{2+} site with center of symmetry. Luminescent ions occupy the lattice sites with inversion symmetry exhibit a longer decay time and the same occupy the center of symmetry sites has a shorter decay time, which is evident in the case of BaSiF$_6$, where Mn^{4+} occupying Si^{4+} sites with a slow decay time in the order of micro- to milliseconds, whereas the RE^{3+} ions occupying Ba^{2+} has a fast decay time in the order of nanoseconds to subnanoseconds.[22,50] The average decay time observed in the present study on binary and ternary doped BGF nanowires (0.3–0.75 ns) is shorter than the decay time reported for codoped BaSiF$_6$ (0.8–1.0 ns) and BaF$_2$ (1.5–2.5 ns) nanowires, in our previous study.[22]

The difference in the decay time of BaSiF$_6$ and BaGeF$_6$ nanophosphors is possibly due to the slightly different in their lattice distortions associated to the size difference of Si^{4+} (54 Å) and Ge^{4+} (67 Å) ions. One can appreciate the influence of the

Table 2 Parameters of exponential fit and average life time of codoped BGF nanowires

Sample	α_1	τ_1 (ns)	α_2	τ_2 (ns)	α_3	τ_3 (ns)	Adj. R^2	Decay time from the plots (ns)
BGF:1Ce–5Tb	513.15	0.381	402.52	2.89	25.12	38.92	0.99332	0.54
BGF:1Ce–10Tb	688.84	0.169	277.54	2.77	33.4	75.16	0.98545	0.32
BGF:1Ce–15Tb	708.61	0.137	251.14	2.21	32.32	74.14	0.97892	0.31
BGF:1Ce–20Tb	704.3	0.198	269.98	2.1	31.16	78.1	0.98289	0.37
BGF:1Ce–30Tb	730.53	0.157	232.87	2.476	32.84	111.36	0.97839	0.27
BGF:3Ce–10Tb	923.38	0.259	143.83	3.026	27.099	133.01	0.96734	0.32
BGF: 1Ce–15Tb–0.01Sm	601.81	0.204	347.33	2.65	31.57	126.05	0.98887	0.58
BGF: 1Ce–15Tb–0.05Sm	607.24	0.19	344.25	2.309	36.469	114.11	0.98658	0.62
BGF:1Ce–20Tb–0.05Sm	744.12	0.693	266.27	3.616	13.99	108.53	0.99648	1.57
BGF:1Ce–30Tb–0.05Sm	711.07	0.954	270.61	3.69	7.87	203.64	0.99718	2.63
BGF: 1Ce–15Tb–0.1Sm	655.21	0.516	343.89	3.183	25.915	131.13	0.99287	0.72
BGF: 1Ce–15Tb–0.5Sm	555.2	0.292	381.55	2.87	40.16	141.86	0.99018	0.75

above difference in ionic radii on crystal lattice on comparing the lattice parameters of $BaSiF_6$ ($a = 4.851$ Å, $\alpha = 98.206°$) and $BaGeF_6$ ($a = 4.948$ Å, $\alpha = 98.245°$) unit cells, with a dissimilarity of 0.1668 on a scale of 0.75.[51] Considering BGF:1Ce–yTb nanowires, the transitions $^5D_4 \rightarrow {}^7F_6$ (488 nm) and $^5D_4 \rightarrow {}^7F_5$ (at 544 nm) are electric-dipole allowed and magnetic-dipole allowed transitions, respectively.[52] The ratio of electric dipole to magnetic dipole transition is a measure of local symmetry surrounding the Tb^{3+} ions as the electric dipole transitions are sensitive to the local symmetry of the dopant site,[53] which is slightly higher in $BaSiF_6$ nanowires. This higher ratio reveals higher symmetry of the dopant ions in the $BaSiF_6$ lattice than those in the $BaGeF_6$ lattice, and therefore a fast decay is expected, which is presumably similar to the reduction in decay time under high pressure due to the change in the local symmetry of the luminescent dopant ions.[54]

Cathodoluminescence characteristics

The CL spectra of the pure and codoped BGF nanowires are recorded under 10 kV and 100 nA electron beam, aimed to simulate the response of the nanowires towards high-energy radiation. The characteristic CL emission spectra are shown in Fig. 9a and b. The pure BGF nanowires emits a broad visible spectrum in the wide range of 300–750 nm when excited by an electron beam. Even though, there was no significant emission in PL studies, pure BGF samples exhibit CL emission. The CL emission in pure lattice is originated by the propagation of ionization initiated by the fast-primary electrons. Upon excitation, the primary electrons create secondary electrons and these secondary electrons leads to more ionization and continues to produce more secondary electrons. Ultimately the cloud of secondary electrons forms and excite the host lattice to generate visible emissions[55] and hence, the luminescent mechanism and therefore the emission characteristics are different between PL and CL.[46] In PL, the energy of photons used are only around 4–6 eV. However, for CL, the energy of fast electrons is 10 kV. Moreover, the CL emission recorded here are from a small area as compared with PL spectra and therefore the excitation energy on a single particle is much higher in CL. The ultraviolet and/or visible light usually excite the activator directly; the fast electrons as high-energy particles always excite the host lattice.[55]

In the CL spectra of BGF:1Ce–yTb and BGF:1Ce–15Tb–zSm nanowires, the emission peaks originated from the host lattices are completely disappeared. The CL spectra of BGF:1Ce–yTb nanowires comprises the most intense emission lines at 544 nm, which is due to the Tb^{3+} ions as in the PL spectra. Since the emissions from the Ce^{3+} ions are completely disappeared in the CL spectra, the energy transfer from the host lattice to Ce^{3+} and then to Tb^{3+} ions are clearly recognized. All the possible transitions of Tb^{3+} are clearly visible in the CL spectra, which does not appear in the PL spectra. The several small peaks in the blue region <450 nm is due to $^5D_3 \rightarrow {}^7F_j$ ($j = 6, 5, 4, 3$) transitions and the peaks in green region >450 are due to $^5D_4 \rightarrow {}^7F_j$ ($j = 6, 5, 4, 3$) transitions of Tb^{3+} ions.[55] The emission bands from Sm^{3+} ions are appeared in BGF:1Ce–15Tb–zSm nanowires, as shown in Fig. 9b. The strong emission lines characteristic to
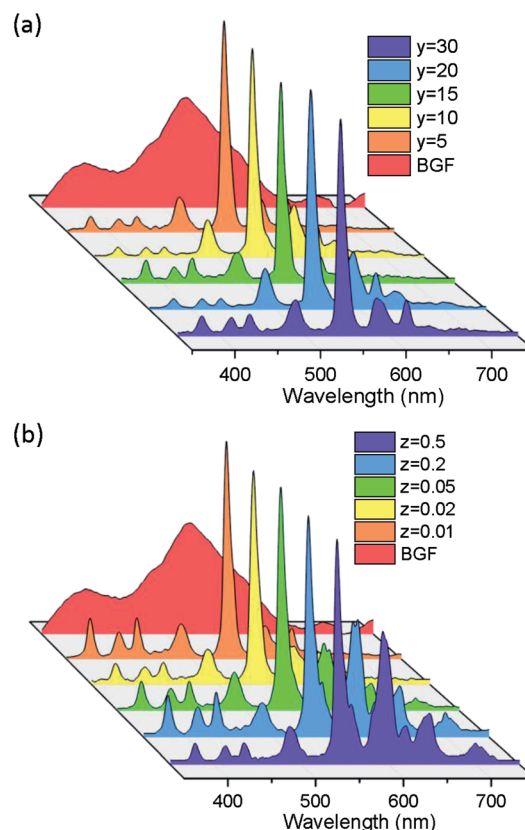

Fig. 9 Cathodoluminescent emission of BGF:1Ce–yTb and (b) BGF:1Ce–15Tb–zSm nanowires.

Tb^{3+} ions in all the CL spectra are due to the high doping level. Moreover, the emission intensities from Sm^{3+} ions in ternary doped BGF nanowires are remarkable though the level of doping of those ions is very minuscule and it is enhanced with the increase of Sm^{3+} content. The emission from Tb^{3+} and Sm^{3+} ions from these ternary doped nanowires are independent since the emission from Tb^{3+} ions are not compromised as observed in the PL spectra. Therefore, in the CL spectra of ternary doped nanowires, the simultaneous emission from both Tb^{3+} and Sm^{3+} ions are possibly due to the contemporary energy transfer to these ions from Ce^{3+} ions. The overall CL emission mechanism from the doped nanowires can be depicted as follows. The secondary electrons excite the host lattice and create many electron–hole pairs, leading to the formation of bound excitons. As no luminescence from bound exciton recombination is observed, these excitons, if formed, decay non-radiatively through a resonant or quasi-resonant transfer to the 4f shell of Sm^{3+} and/or Tb^{3+} ions and give their characteristic emission.[56]

Additionally, the CIE coordinates from the CL spectra of the nanowires are calculated and presented in Table 3. From the CIE diagram shown in Fig. S11,† majority of the nanowires exhibit an overall emission in green-orange region. It is obvious that the Ce^{3+}–Tb^{3+} codoped nanowires expected to emit a green light and the Ce^{3+}–Tb^{3+}–Sm^{3+} codoped nanowires to emit orange light and the same can be observed in the chromaticity diagram.

Table 3 CIE Coordinates calculated from the CL spectra of codoped BGF nanowire phosphors

Sl no.	Sample composition	CIE (x)	CIE (y)
1	BGF:1Ce–10Tb	0.3281	0.5205
2	BGF:2Ce–10Tb	0.3745	0.5164
3	BGF:1Ce–15Tb	0.3193	0.4910
4	BGF:1Ce–20Tb	0.3745	0.5162
5	BGF:1Ce–30Tb	0.3334	0.4970
6	BGF: 1Ce–15Tb–0.01Sm	0.3167	0.4724
7	BGF: 1Ce–15Tb–0.02Sm	0.3425	0.4947
8	BGF: 1Ce–15Tb–0.05Sm	0.3764	0.4806
9	BGF:1Ce–20Tb–0.05Sm	0.4244	0.4347
10	BGF:1Ce–30Tb–0.05Sm	0.3913	0.4778
11	BGF:1Ce–15Tb–0.1Sm	0.4058	0.4480
12	BGF:1Ce–15Tb–0.5Sm	0.4044	0.3711

Photoluminescence sensitivity towards H_2O_2 detection

The synthesized ternary RE^{3+} doped BGF nanowires are used as luminescent probe for the detection of H_2O_2, which is a model for the reactive oxygen species.[57] The sensing performance of representative BGF:1Ce–15Tb–0.05Sm nanophosphors dispersed in water is tested by recording the fluorescent spectra in the presence of different concentrations of H_2O_2 (con. H_2O_2), as shown in Fig. 10a. The PL spectra for different con. H_2O_2 ranging from 25 μM to 3000 μM, clearly show a change in fluorescence nature of BGF:1Ce–15Tb–0.05Sm nanowires with respect to con. H_2O_2 even at the low concentrations. The calibration curve in the inset of Fig. 10a indicates that the relative fluorescence intensity (I/I_0) has a logarithmic relationship $I/I_0 = 1.484 - 0.184 \times \ln(\text{con. } H_2O_2)$, where I and I_0 are the fluorescence intensity in the presence and absence of H_2O_2, respectively. The corresponding calculated and residual values of the fit is presented in Table S2.† As shown in Fig. 10b, the quenching efficiency, defined as $QE = (I_0 - I)/I_0 \times 100\%$, obviously depicts that the increase in the H_2O_2 concentration x enhances the QE with the following relationship (the calculated and residual values are presented in Table S3†):

$$QE = -48.36 + 18.39 \times \ln(\text{con. } H_2O_2) \quad (4)$$

The intensity of all transitions of Sm^{3+} are decreased simultaneously in the presence of H_2O_2, when excited by 254 nm source. The sensor is not only highly sensitive, it is also quantitative for x between 25–3000 ppm. Furthermore, the detection selectivity was tested with glucose, Fe^{3+}, Cu^{2+}, and pH, as shown in Fig. 10c. Their addition to BGF:1Ce–15Tb–0.05Sm dispersion leads to negligible modifications to the luminescence intensity (<5%), whereas the addition of H_2O_2 leads to a >40% decrease. This reveals the good selectivity of the sensor. The reduction in the intensity of the Sm^{3+} emission from the BGF:1Ce–15Tb–0.05Sm nanowires only in the presence of H_2O_2 can be attributed to the oxidation of Ce^{3+} to Ce^{4+} by eqn (5). Besides, Ln^{3+} ions in aqueous solutions exhibit a strong affinity towards negatively charged oxygen.[58]

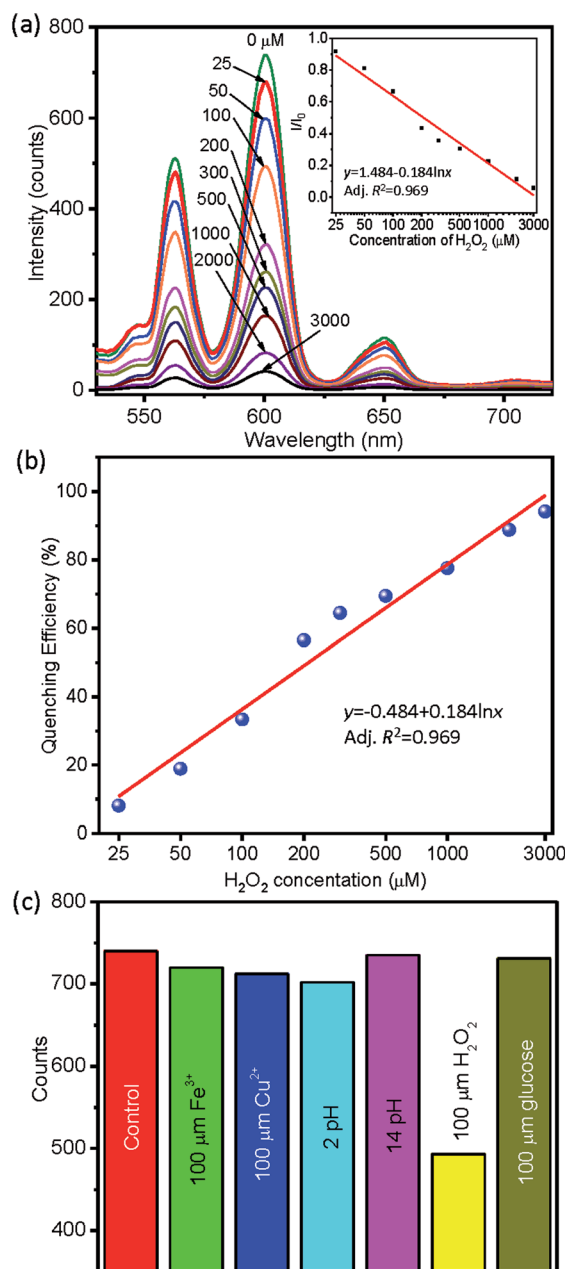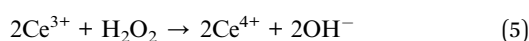$$2Ce^{3+} + H_2O_2 \rightarrow 2Ce^{4+} + 2OH^- \quad (5)$$

Fig. 10 (a) PL response of nanowires towards H_2O_2 concentration, calibration curve is in the inset, (b) quenching efficiency, and (c) selectivity of BGF nanowires towards H_2O_2.

With an increase of Ce^{4+} ions, the actual charge transfer bridge between Ce^{3+}, Tb^{3+} and Sm^{3+} is disrupted and ultimately the intensity of emissions from Sm^{3+} ions are decreased.

The sensitivity of binary doped green emitting BGF:1Ce–30Tb and representative binary (Ce^{3+} and Tb^{3+}) and ternary (Ce^{3+}, Tb^{3+} and Eu^{3+}) doped $BaSiF_6$ nanowires towards H_2O_2 are further studied and presented in Fig. S12.† In both the cases, the ternary doped nanowires are more sensitive than their binary doped counterparts, which reveals that the low concentration of sensitizer ions (Sm^{3+} or Eu^{3+}) are favorable for effective sensing of H_2O_2 using these nanowires. On comparing the sensitivity towards H_2O_2 between BGF and $BaSiF_6$ nanowires,

BGF nanowires are more sensitive towards H_2O_2. Moreover, the binary doped BGF nanowires display more sensitivity than the ternary doped $BaSiF_6$ nanowires (Fig. S12d†). Hence, codoped BGF nanowires are promising for the detection of H_2O_2 at the low concentrations. In addition, the sensitivity and detection limit may be further optimized by controlling the level of dopants in the nanowires and the content of nanowires in the water dispersion.[59]

Conclusions

A pure phase BGF nanowires with high aspect ratios was fabricated through a solvothermal method. The nanowires exhibited visible PL emissions when codoped with varying Ce^{3+}, Tb^{3+}, and Sm^{3+} rare-earth ions, under 254 nm excitation. The XRD analysis revealed the crystalline nature of the nanowires with rhombohedral structure and the structure type is not affected by the rare-earth dopants. The PL emission monitored when excited by 254 nm source is related to the energy transfer between Ce^{3+}–Tb^{3+}–Sm^{3+} ions. The visible emission from the codoped BGF nanowires when excited by 350 nm source was also recorded. The decay time of codoped BGF nanowires was found to be very short in the order of subnanoseconds, which is one of the shortest decay time records observed so far. The strong visible CL emission from the BGF nanowires reveals their potential use for the field emission displays and the detection of high-energy radiation. The visible PL emissions from the ternary doped BGF nanowires are sensitive to H_2O_2 at low concentrations and thus they can be used for H_2O_2 detection with high sensitivity.

Authors' contributions

G. George conducted the sample synthesis, and PL and EPMA/CL measurements, and prepared the manuscript; M. D. Simpson conducted the sample processing and preparation; B. R. Gautam conducted the decay dynamics; D. Fang attended the experimental design and data analysis; J. Peng, and J. Wen conducted the TEM work; J. E. Davis and D. Ila conducted the research on scintillation; and Z. Luo designed the experiment, analysed the experimental data and revised the manuscript.

Conflicts of interest

There are no conflicts to declare.

Acknowledgements

References

1 Y. S. Zhao, P. Zhan, J. Kim, C. Sun and J. Huang, *ACS Nano*, 2010, **4**, 1630–1636.
2 X. Wang, C. J. Summers and Z. L. Wang, *Nano Lett.*, 2004, **4**, 423–426.
3 J. H. He, R. S. Yang, Y. L. Chueh, L. J. Chou, L. J. Chen and Z. L. Wang, *Adv. Mater.*, 2006, **18**, 650–654.
4 Z. Luo, J. G. Moch, S. S. Johnson and C. C. Chen, *Curr. Nanosci.*, 2017, **13**, 364–372.
5 Y. Huang, H. You, G. Jia, Y. Song, Y. Zheng, M. Yang, K. Liu and N. Guo, *J. Phys. Chem. C*, 2010, **114**, 18051–18058.
6 Y.-P. Du, X. Sun, Y.-W. Zhang, Z.-G. Yan, L.-D. Sun and C.-H. Yan, *Cryst. Growth Des.*, 2009, **9**, 2013–2019.
7 E. Nieboer, C. K. Jørgensen, R. D. Peacock and R. Reisfeld, *Rare Earths*, Springer-Verlag, Berlin Heidelberg, 1975.
8 D. J. Naczynski, M. C. Tan, M. Zevon, B. Wall, J. Kohl, A. Kulesa, S. Chen, C. M. Roth, R. E. Riman and P. V. Moghe, *Nat. Commun.*, 2013, **4**, 2199.
9 S. Wang, J. Feng, S. Song and H. Zhang, *CrystEngComm*, 2013, **15**, 7142–7151.
10 C. Altavilla, *Upconverting Nanomaterials: Perspectives, Synthesis, and Applications*, CRC Press, Boca Raton, 2016.
11 N. Kumam, L. P. Singh, S. K. Srivastava and N. R. Singh, *J. Lumin.*, 2018, **203**, 59–66.
12 Q. Zhou, Y. Zhou, F. Lu, Y. Liu, Q. Wang, L. Luo and Z. Wang, *Mater. Chem. Phys.*, 2016, **170**, 32–37.
13 D. Sekiguchi and S. Adachi, *Opt. Mater.*, 2015, **42**, 417–422.
14 Y. Zhou, Q. Zhou, Y. Liu, Z. Wang, H. Yang and Q. Wang, *Mater. Res. Bull.*, 2016, **73**, 14–20.
15 R. Hoshino, T. Nakamura and S. Adachi, *ECS J. Solid State Sci. Technol.*, 2016, **5**, R37–R43.
16 Q. Zhou, H. Tan, Q. Zhang, N. Wang, Q. Wei, Z. Wang, M. Rong and Q. Wang, *RSC Adv.*, 2017, **7**, 32094–32099.
17 H. F. Sijbom, R. Verstraete, J. J. Joos, D. Poelman and P. F. Smet, *Opt. Mater. Express*, 2017, **7**, 3332–3365.
18 S. Adachi and T. Takahashi, *J. Appl. Phys.*, 2009, **106**, 013516.
19 T.-C. Lang, T. Han, L.-L. Peng and M.-J. Tu, *Mater. Chem. Front.*, 2017, **1**, 928–932.
20 Z. Wang, Y. Liu, Y. Zhou, Q. Zhou, H. Tan, Q. Zhang and J. Peng, *RSC Adv.*, 2015, **5**, 58136–58140.
21 Y. K. Xu and S. Adachi, *J. Electrochem. Soc.*, 2011, **158**, J58–J65.
22 G. George, S. L. Jackson, Z. R. Mobley, B. R. Gautam, D. Fang, J. Peng, D. Luo, J. Wen, J. E. Davis, D. Ila and Z. Luo, *J. Mater. Chem. C*, 2018, **6**, 7285–7294.
23 Q. Zhou, Y. Zhou, Y. Liu, L. Luo, Z. Wang, J. Peng, J. Yan and M. Wu, *J. Mater. Chem. C*, 2015, **3**, 3055–3059.
24 F. Hong, H. Cheng, G. Liu, X. Dong, W. Yu and J. Wang, *Inorg. Chem.*, 2018, **57**, 9892–9901.
25 R. A. B. Silva, R. H. O. Montes, E. M. Richter and R. A. A. Munoz, *Food Chem.*, 2012, **133**, 200–204.
26 I. Kim, N. Yamashita and H. Tanaka, *J. Hazard. Mater.*, 2009, **166**, 1134–1140.

27 M. Schäferling, D. B. M. Grögel and S. Schreml, *Microchim. Acta*, 2011, **174**, 1.

28 J. Bogacki, P. Marcinowski, E. Zapałowska, J. Maksymiec and J. Naumczyk, *Environ. Technol.*, 2017, **38**, 2589–2600.

29 S. G. Rhee, *Science*, 2006, **312**, 1882–1883.

30 Y. Wang, J. Huang, C. Zhang, J. Wei and X. Zhou, *Electroanalysis*, 1998, **10**, 776–778.

31 N. Luo, G. H. Miley, R. J. Gimlin, R. L. Burton, J. Rusek and F. Holcomb, *J. Propul. Power*, 2008, **24**, 583–589.

32 M. E. Germain and M. J. Knapp, *Inorg. Chem.*, 2008, **47**, 9748–9750.

33 G. Brauer, *Handbook of Preparative Inorganic Chemistry*, Academic Press, London, 1963, vol. 1.

34 J. L. Hoard and W. B. Vincent, *J. Am. Chem. Soc.*, 1940, **62**, 3126–3129.

35 D. Gantar, A. Rahten and B. Volavšek, *Thermochim. Acta*, 1985, **96**, 207–212.

36 T. E. Mallouk, B. Desbat and N. Bartlett, *Inorg. Chem.*, 1984, **23**, 3160–3166.

37 C. Lorbeer, F. Behrends, J. Cybinska, H. Eckert and A.-V. Mudring, *J. Mater. Chem. C*, 2014, **2**, 9439–9450.

38 E. van der Kolk, P. Dorenbos, C. W. E. van Eijk, A. P. Vink, C. Fouassier and F. Guillen, *J. Lumin.*, 2002, **97**, 212–223.

39 B. F. Aull and H. P. Jenssen, *Phys. Rev. B*, 1986, **34**, 6640–6646.

40 C. Duan, Z. Zhang, S. Rösler, S. Rösler, A. Delsing, J. Zhao and H. T. Hintzen, *Chem. Mater.*, 2011, **23**, 1851–1861.

41 H. Yin, Y. Li, J. Bai, M. Ma and J. Liu, *J Materiomics.*, 2017, **3**, 144–149.

42 M. G. Ha, J.-S. Jeong, K.-R. Han, Y. Kim, H.-S. Yang, E. D. Jeong and K. S. Hong, *Ceram. Int.*, 2012, **38**, 5521–5526.

43 Z. Xia and W. Wu, *Dalton Trans.*, 2013, **42**, 12989–12997.

44 P. I. Paulose, G. Jose, V. Thomas, N. V. Unnikrishnan and M. K. R. Warrier, *J. Phys. Chem. Solids*, 2003, **64**, 841–846.

45 G. Seeta Rama Raju and J. S. Yu, *Spectrochim. Acta, Part A*, 2014, **124**, 383–388.

46 G. Blasse and B. C. Grabmaier, *Luminescent Materials*, Springer-Verlag, Berlin Heidelberg, 2012.

47 X. Zhang and M. Gong, *Ind. Eng. Chem. Res.*, 2015, **54**, 7632–7639.

48 W. Lü, H. Xu, J. Huo, B. Shao, Y. Feng, S. Zhao and H. You, *Dalton Trans.*, 2017, **46**, 9272–9279.

49 L. Wang, R.-J. Xie, T. Suehiro, T. Takeda and N. Hirosaki, *Chem. Rev.*, 2018, **118**, 1951–2009.

50 D. Sekiguchi, J. Nara and S. Adachi, *J. Appl. Phys.*, 2013, **113**, 183516.

51 K. Persson, *Materials Data on BaSiF$_6$ (SG:166) by Materials Project*, 2014, DOI: 10.17188/1270502.

52 T. R. Faulkner and F. S. Richardson, *Mol. Phys.*, 1978, **36**, 193–914.

53 J. J. H. A. van Hest, G. A. Blab, H. C. Gerritsen, C. de Mello Donega and A. Meijerink, *J. Phys. Chem. C*, 2017, **121**, 19373–19382.

54 A. Lazarowska, S. Mahlik, M. Grinberg, G. Li and R.-S. Liu, *Sci. Rep.*, 2016, **6**, 34010.

55 X. Liu and J. Lin, *J. Mater. Chem.*, 2007, **18**, 221–228.

56 P. T. Diallo, P. Boutinaud, R. Mahiou and J. C. Cousseins, *Phys. Status Solidi A*, 1997, **160**, 255–263.

57 E. J. Pereira, C. M. Smolko and K. A. Janes, *Front. Pharmacol.*, 2016, **7**, 457.

58 F. S. Richardson, *Chem. Rev.*, 1982, **82**, 541–552.

59 N. Duée, C. Ambard, F. Pereira, D. Portehault, B. Viana, K. Vallé, D. Autissier and C. Sanchez, *Chem. Mater.*, 2015, **27**, 5198–5205.